Research Square

Preprints are preliminary reports that have not undergone peer review.
They should not be considered conclusive, used to inform clinical practice,
or referenced by the media as validated information.

Nickel Metalation and Ni-Cluster Nodes Regulate Reactive Oxygen Species Generation in a Stacked Nanosheet Porphyrinic MOF for Antibacterial Photocatalysis

Aswathy Kaiprampattuparambil Gopi
Cochin University of Science and Technology
Surya Rao
Cochin University of Science and Technology
Krishnendu Madhu
Cochin University of Science and Technology
Adarsh Karott Joy
Cochin University of Science and Technology
Fazalurahman Kuttassery
University of Calicut
Hiroshi Tachibana
Tokyo Metropolitan University
Haruo Inoue
Tokyo Metropolitan University
Sebastian Nybin Remello
nybinremello@cusat.ac.in

Cochin University of Science and Technology

Research Article

Keywords: Nickel-Porphyrin MOF, Photocatalytic antibacterial activity, Singlet oxygen generation, Type-I & Type-II PDT

Posted Date: November 17th, 2026

DOI: https://doi.org/10.21203/rs.3.rs-11458221/v1

License: This work is licensed under a Creative Commons Attribution 4.0 International License.
Read Full License

Additional Declarations: No competing interests reported.

Abstract

The emergence of multidrug-resistant bacteria has created an urgent need for alternative antimicrobial strategies that circumvent conventional antibiotic resistance mechanisms. Herein, we report a visible-light-responsive porphyrinic nickel metal-organic framework (NiTCPP MOF) constructed from tetrakis(4-carboxyphenyl)porphyrin (TCPP) linkers and nickel-based secondary building units for photocatalytic bacterial inactivation. Structural and spectroscopic analyses revealed partial in situ nickel metalation of the porphyrin linkers, leading to modified excited-state dynamics and enhanced photodynamic activity. Under visible-light irradiation, the NiTCPP MOF achieved near-complete inactivation of *Salmonella typhimurium*. Mechanistic investigations indicate that antibacterial activity is governed primarily by a Type-II photodynamic pathway, in which nickel metalation enhances spin-orbit coupling, promotes intersystem crossing, and facilitates efficient singlet oxygen generation. Simultaneously, the redox-active Ni-cluster nodes promote photoinduced charge separation and photocatalytic oxygen reduction, giving rise to a secondary Type-I pathway associated with H_2O_2 production. In addition, photogenerated holes may contribute to bacterial inactivation through the direct oxidation of membrane constituents and intracellular biomolecules. The synergistic action induces severe oxidative stress, resulting in bacterial cell damage and inactivation. These findings demonstrate how linker-centered photodynamic processes and node-centered photocatalytic reactions can be integrated within a single MOF architecture to enhance reactive oxygen species generation and antibacterial performance, highlighting NiTCPP MOFs as promising materials for antimicrobial applications.

Introduction

Antimicrobial resistance (AMR) has become a major global health concern, which poses significant socioeconomic burdens worldwide, threatening the effectiveness of conventional antibiotic therapies.[1] The widespread misuse and overuse of antibiotics have resulted in the emergence of multidrug-resistant (MDR) pathogens, leading to the development of bacterial strains which are capable of evading nearly all clinically available antimicrobial drugs.[2] Moreover, the formation of bacterial biofilms significantly aggravates the problem, as the extracellular polymeric matrix acts as a protective barrier that impedes the antibiotic penetration and enhances the bacterial tolerance toward the host immune responses.[3] Consequently, the development of alternative antimicrobial strategies that can effectively eradicate both the planktonic bacteria and the biofilm-associated infections while minimizing the antimicrobial resistance has become an urgent scientific priority.[4] Photocatalytic bacterial inactivation, driven by light, has emerged as a prominent non-antibiotic therapeutic approach owing to its broad-spectrum antibacterial efficacy, minimal invasiveness, precise activation control, and negligible potential for inducing bacterial resistance.[5–7] In contrast to the conventional antibiotics which target specific metabolic pathways, the photocatalytic antibacterial systems relies on the generation of highly reactive oxygen species (ROS) capable of simultaneously attacking multiple cellular targets.[8]

Metal-organic frameworks (MOFs) have emerged as highly promising materials for advanced visible-light-responsive photocatalytic antibacterial activity. Their exceptionally high surface area, structural diversity, tunable pore structure, and chemical functionalities provide significant opportunities for engineering MOFs as photocatalytic and photodynamic platforms.[9–11] Among the various photoactive MOFs, porphyrin-containing MOFs have garnered significant interest owing to the high molar absorption coefficients and excellent singlet oxygen quantum yields of porphyrin macrocycles.[12–15] The integration of porphyrin macrocycles into the MOF framework can effectively suppress their aggregation-induced quenching by spatially isolating the molecules with an ordered crystalline framework.[16] This framework confinement strategy conserves the inherent photophysical properties of porphyrin macrocycles while simultaneously enhancing light harvesting, oxygen accessibility, and ROS production. Consequently, porphyrin-based MOFs combine the superior photosensitizing characteristics of porphyrins with the structural advantages of MOFs, creating platforms for photocatalytic antibacterial application. Recent studies have demonstrated the versatility of porphyrin-based MOFs for photocatalytic bacterial inactivation. For instance, Xu et al. reported a Cu-TCPP MOF nanoflower exhibiting high visible-light-responsive antibacterial activity through ROS-mediated photodynamic and photothermal pathways, showing broad-spectrum activity against both bacteria and fungi.[17] Recently, Shivam et al. reported a Zn-porphyrin terephthalate mixed-linker MOF that exhibited enhanced ROS generation and antibacterial activity against both MRSA and E. coli under red-light irradiation.[18] In another study, Feng et al. constructed a Nano-PCN-222(Fe) MOF nanozyme with peroxidase-like activity, where the Fe-centers catalysed the conversion of H_2O_2 into highly reactive hydroxyl radicals.[19] These studies demonstrate the potential of porphyrin-based MOFs for ROS-mediated photobacterial inactivation through the synergistic contributions of photoactive porphyrin ligands and redox metal centers. Although a nickel-tetraniline coordination framework with biomedical applications has been reported by Hiremath et al.[20], introductions of Ni to both cluster nodes and light absorbing linkers have not been reported: How the Ni-cluster nodes and the strongly light absorbing Ni-porphyrin linkers behave in the excited-state dynamics to exhibit synergetic effect on ROS generation pathways would be most interesting to be studied.

In this study, we present the hydrothermal synthesis of a layered porphyrin-based nickel metal-organic framework (NiTCPP MOF), constructed from photoactive tetrakis(4-carboxyphenyl) porphyrin (TCPP) and nickel secondary building units, for photocatalytic bacterial inactivation to find that dual modes of ROS generation through Type 1 and II pathways are effectively operating. The photocatalytic inactivation potential of the NiTCPP MOF was assessed by inhibiting the growth of *S. typhimurium* under light irradiation. Singlet oxygen trapping assay and oxygen reduction reaction (ORR) studies were conducted to elucidate the disinfection mechanism.

MATERIALS AND METHODS

Chemicals and Reagents

All chemicals and reagents used in this study were commercially obtained and used without further purification. 5,10,15,20-tetrakis(4-carboxyphenyl) porphyrin (TCPP > 99.0%) and oxo[5,10,15,20-tetra(4-pyridyl)porphyrinato]titanium(IV) (TiTPyP > 90.0%) were purchased from TCI Japan. Nickel (II) acetate tetrahydrate (Ni $(CH_3COO)_2 \cdot 4H_2O$ > 97.0%), methanol (MeOH) (> 99.8%), and dimethylformamide (DMF) (> 99.0%) were purchased from Spectrochem India Pvt. Ltd. Ethanol (EtOH) (> 99.9%) was purchased from Changshu Hongsheng Fine Chemicals. Benzoic acid (≥ 99.5%), perfluorinated resin containing nafion (10 wt. % in H_2O) and anthracene-9-carboxylic acid (> 95%) were purchased from Merck. Sodium chloride (NaCl) (> 99.0%) was purchased from NICE Laboratory Chemicals. Nutrient Broth and Mueller-Hinton Agar were purchased from HIMEDIA. Deionized water was used in this study.

Material Characterization

Powder X-ray diffraction (PXRD) patterns were obtained using a Bruker AXS D8 Advance diffractometer. A JASCO-4100 FT-IR spectrometer was used to obtain the FT-IR spectra using KBr as the matrix. Morphological characterization was performed using a JSM-6390LV/JED-2300 FESEM with energy-dispersive X-ray spectroscopy (EDS). HR-TEM images were obtained using a JEOL JEM-2100 instrument. N_2 adsorption-desorption isotherms were obtained at 77 K using a Micromeritics ASAP 2420 system. Thermogravimetric analysis was performed using a PerkinElmer STA 6000 instrument. A PHI 5000 Versa Probe II photoelectron spectrometer was used for XPS measurements. DRS spectra were recorded using a PerkinElmer Lambda 365 spectrophotometer. Electrochemical characterization, such as EIS, Mott-Schottky, and CV plots, was performed using an ALS/CH electrochemical analyzer (Model 611 DST). Photoluminescence (PL) and time-resolved photoluminescence (TRPL) spectra were acquired using a Horiba Fluorolog-3 Fluorescence spectrometer. A 100 W xenon lamp was used for the photobacterial study, whereas a 420 nm monochromatic LED (3.5 mW/cm^2) was used for the singlet oxygen trapping assay.

Synthesis of NiTCPP MOF

NiTCPP MOF was synthesized using a hydrothermal method, where, 5,10,15,20-tetrakis(4-carboxyphenyl) porphyrin (TCPP, 0.11 mmol), nickel (II) acetate tetrahydrate ($Ni(CH_3COO)_2 \cdot 4H_2O$, 0.313 mmol), and benzoic acid (17.03 mmol) were ultrasonically dissolved in a DMF: H_2O mixture (14:2 v/v) and subsequently transferred into a 20 mL Pyrex vial. The sealed vial was then heated at 120°C for 12 h in a gravity convection oven. After the reaction was complete, the reddish-purple crystalline material was collected by filtration and thoroughly washed with fresh DMF. Subsequently, solvent exchange was performed using methanol to replace the residual DMF. The obtained crystals were activated by drying at 80°C for 1 h.

NiTCPP MOF Electrode Preparation

For the electrochemical characterization, working electrode was prepared by dispersing approximately 5 mg of NiTCPP MOF in a mixture of 50 µL Nafion and 450 µL ethanol. The resultant mixture was then ultrasonicated to obtain a homogeneous suspension and drop-casted onto a clean fluorine-doped tin oxide (FTO) glass plate with an active area of 1 × 1 cm^2. Subsequently, the coated electrode was dried at 60°C for 15 minutes to enhance the adhesion of the material.

Photocatalytic Antibacterial Study

Prior to the experiment, all disks and the NiTCPP MOF were autoclaved for sterilization. The photoactivity of the NiTCPP MOF was evaluated using *Salmonella typhimurium MTCC 3224.* For the experiment, the bacterial cultures were grown in nutrient broth at 37°C for 18 h to obtain a cell density of approximately 10^7 CFU mL^{-1}. The bacterial cells were centrifuged at 6000 rpm for 5 min and then reintroduced into a sterile saline solution with a concentration of 0.9% (w/v). The bacterial suspension was subsequently diluted with sterile saline to obtain a concentration of 10^5 CFU mL^{-1}. For the antibacterial photodegradation study, 10 mg of NiTCPP MOF was dispersed in 10 mL of a bacterial suspension (10^7 CFU mL^{-1}) contained in a 20 mL photoreactor. The bacterial suspension was continuously stirred at room temperature while irradiated with a 100 W xenon lamp (100 mW cm^{-2}). After 120 min of light irradiation, aliquots of the bacterial suspension were withdrawn and serially diluted as required. The standard spread plate method was adopted to quantify the bacterial population. The agar plates were incubated at 37°C for 24 h after inoculation.

Singlet Oxygen Trapping Assay

Singlet oxygen ($^1O_2$) generation was evaluated using anthracene-9-carboxylic acid as a chemical trap. For the experiment, 10 mg of NiTCPP MOF was dispersed in 25 mL of a 1.5mM anthracene-9-carboxylic acid solution in acetonitrile. The reaction mixture was irradiated with monochromatic 420 nm light under continuous stirring at RT. At regular intervals, aliquots of the reaction mixture were withdrawn, the MOF was removed by centrifugation, and the absorbance was measured using a UV–Vis spectrophotometer.

Photocatalytic Oxygen Reduction Reaction

The photocatalytic oxygen reduction reaction (ORR) was carried out by dispersing 10 mg of NiTCPP MOF in10 mL of deionized water or in a water: methanol mixture (8:2, v/v). The suspension was then irradiated with a white LED lamp for 5 h under continuous magnetic stirring in the dark. Upon completion of the reaction, the NiTCPP MOF was removed by filtration, and 2 mL of 1 M H_2SO_4 was added to acidify the reaction mixture.

For hydrogen peroxide detection, 1 mL of the acidified reaction solution was added to 500 µL of TiTPyP solution prepared in H_2SO_4 and kept stirring in the dark for 1 h to ensure complete reaction between

TiTPyP and H_2O_2. The UV-Vis absorption spectrum of the solution was subsequently recorded, and the presence of H_2O_2 was analyzed by the change in the characteristic absorbance of TiTPyP.[21–23]

RESULTS AND DISCUSSION

Structural Characterization of NiTCPP MOF

The crystalline structure of the as-synthesized NiTCPP MOF was examined using powder X-ray diffraction (PXRD), as shown in Fig. 1(a). The PXRD results revealed a well-defined sharp diffraction peak, confirming the formation of a highly crystalline structure. The prominent diffraction peak observed at a low diffraction angle (7.8°) indicates the presence of a periodic mesoporous structure[24] while the additional intense reflections centered around 20° are characteristic of layered metal-organic frameworks.[17,25,26] Moreover, the narrow peak widths and high peak intensities suggest the good crystallinity and structural homogeneity of the synthesized framework.

FTIR spectroscopy further verified the framework formation by confirming the presence of new peaks corresponding to TCPP-Ni cluster coordination. As depicted in Fig. 1(b), the TCPP ligand exhibited a characteristic absorption band at 1656 cm^{-1}, corresponding to the stretching vibration of the free carboxylic acid (-COOH) groups in the porphyrin ring. After MOF formation, this peak disappeared completely, and two new peaks corresponding to the asymmetric and symmetric stretching vibrations of the coordinated carboxylate groups (1557 and 1490 cm^{-1}, respectively) appeared. The presence of these distinctive carboxylate vibrations, along with the absence of the -COOH peak, indicates the successful coordination of the TCPP ligand to the nickel cluster nodes.[27] The bands at 1400 and 1114 cm^{-1} are attributed to the phenolic C-C and C-O stretching frequencies. The peaks observed below 1100 cm^{-1} were ascribed to the stretching frequencies associated with the Ni metal cluster.

The material morphology was further investigated using SEM and TEM (Fig. 2(a-d)). The SEM observations were in excellent agreement with the PXRD results, as the images revealed the formation of well-defined cuboid-like crystals composed of multiple stacked layers. Distinct parallel lamellar were clearly observed throughout the material, resembling a book-like architecture constructed from thin nanosheets. The stacking arrangement of the framework shows that the material grows preferentially as a nanosheet, followed by an ordered assembly into a three-dimensional hierarchical structure. The uniformity of the layered arrangement suggests strong interlayer interactions, which may arise from π–π stacking interactions between the adjacent porphyrin units.[28]

The elemental composition of the as-synthesized NiTCPP MOF was further investigated using EDS and elemental mapping analyses (Fig. 1S in the Supporting Information). The EDS spectrum confirms the presence of the constituent elements C, N, O, and Ni. The presence of Ni further verified the successful incorporation of metal nodes within the framework structure. Furthermore, elemental mapping analysis revealed a homogeneous distribution of C, N, O, and Ni throughout the entire microcrystal, demonstrating the uniform incorporation of both TCPP and Ni centers within the framework.

The porosity and specific surface area of the NiTCPP MOF were investigated by N_2 adsorption-desorption measurements at 77 K, and the corresponding isotherm and pore size distribution are shown in Fig. 3(a) and (b), respectively. The Brunauer-Emmett-Teller (BET) specific surface area of the NiTCPP MOF was determined to be 173.54 $m^2 g^{-1}$, with a total pore volume of 0.0947 $cm^3 g^{-1}$. The relatively low pore volume further supports the formation of a densely packed, layered crystal structure, as observed in the SEM analysis. Moreover, the adsorption and desorption branches display a small hysteresis loop at higher relative pressures, which can be attributed to capillary condensation occurring within slit-shaped pores formed by the stacking of nanosheets.[29] The pore size distribution analysis further revealed that the as-synthesized NiTCPP MOF possessed an average pore diameter of 2.18 nm, confirming its mesoporous structure. The observed mesoporosity can be attributed to interlayer voids generated during the ordered stacking of two-dimensional MOF nanosheets.

The surface chemical composition and oxidation states of the NiTCPP MOF were further investigated using X-ray photoelectron spectroscopy (XPS), and the corresponding spectra are presented in Fig. 4 (a-d). The survey spectrum (Fig. 2S) exhibits characteristic signals for C, N, O, and Ni, confirming the successful incorporation of porphyrinic ligands and nickel centers within the framework. The high-resolution C1s spectra (Fig. 4(a)) can be deconvoluted into three distinct peaks at 284.7, 287.3, and 288.7 eV, corresponding to C-C/C-H, C-N/C = N, and O-C = O species, respectively.[30,31] These characteristic peaks originate from the conjugated porphyrin framework and carboxylate functionalities of the TCPP linker. The O1s spectrum (Fig. 4(b)) consists of two deconvoluted peaks at 531.9 and 533.3 eV. The lower binding energy peak at 531.9 eV is attributed to the oxygen atoms involved in Ni-O coordination and the C = O groups of the carboxylate ligands, whereas the higher binding energy peak at 533.3 eV corresponds to the C-O bond.[31] These results further verify the coordination of the carboxylate groups of porphyrins with the nickel centers during the framework formation. The high-resolution N 1s spectrum (Fig. 4(c)) displays a prominent peak at 398.3 eV, which is assigned to the Ni-N bond within the porphyrin macrocycle, indicating a partial metalation of porphyrin with Ni during the MOF formation.[31] The high-resolution Ni 2p spectrum (Fig. 4(d)) exhibits two characteristic spin-orbit doublets and their corresponding shake-up satellite peaks. The peaks at 854.7 eV (Ni $2p_{3/2}$) and 871.8 eV (Ni $2p_{1/2}$) are assigned to Ni^{2+} species, while the additional components located at 857.9 (Ni $2p_{3/2}$) and 873.9 (Ni $2p_{1/2}$) eV correspond to Ni^{3+} species.[32]

The thermal stability of the as-synthesized NiTCPP MOF was investigated using thermogravimetric analysis (TGA). Figure 3S shows the TG curve recorded from room temperature to 700°C. The TGA results show three characteristic steps, including weight loss below100 ^{0}C, 200^{o}C and between 400-500^{o}C, which can be attributed to the evaporation of trapped solvent molecules and the decomposition of the framework structure with the dissociation of the Ni-O bond, respectively.

The optical absorption properties of the as-synthesized NiTCPP MOF were analyzed using UV-visible diffuse reflectance spectroscopy (UV-DRS), and the corresponding spectra are shown in Fig. 5 (a). The material exhibited strong absorption throughout the visible-light region, which can be attributed to the

characteristic electronic transitions of porphyrin chromophores. A Tauc plot was used to evaluate the optical bandgap of the material. As shown in Fig. 5(b), the bandgap energy of the NiTCPP MOF was estimated to be approximately 2.0 eV. The Electrochemical impedance spectra of the NiTCPP MOF (Fig. 5(c)) demonstrate that the as-synthesized NiTCPP MOF has a significantly lower semicircle diameter in the high-frequency region than TCPP, indicating a lower charge-transfer resistance and enhanced electrical conductivity. The electronic band levels of the NiTCPP MOF were further investigated using Mott-Schottky analysis (Fig. 5(d)). The positive slope obtained in the Mott-Schottky plot confirmed the *n*-type semiconducting nature of the material, indicating that electrons are the majority charge carriers. The flat-band potential was determined to be approximately − 0.9 V versus Ag/AgCl. For *n*-type semiconductors, the conduction band (CB) is generally considered as the flat-band potential.[33] Accordingly, the CB level of the NiTCPP MOF was calculated to be approximately − 0.7 V vs. NHE. Using the experimentally determined bandgap value of 2.0 eV, the valence band (VB) level was calculated to be approximately + 1.3 V vs. NHE. To explore the photoinduced charge separation and excited-state dynamics of the as-synthesized NiTCPP MOF, PL spectra and lifetime measurements (Fig. 5(e) and (f)) were obtained. Compared to the TCPP ligand, the NiTCPP MOF exhibited significant quenching of the PL emission, indicating that substantial nonradiative processes such as a charge separation into carrier electron/hole pair caused by the photoinduced charge transfer from the porphyrin linker to the Ni clusters and an enhanced intersystem crossing to the triplet manifolds are competing with the ordinary radiative electron-hole recombination following framework formation. The lifetime values further revealed a decrease in the fluorescence lifetime from 10.06 ns for the TCPP ligand to τ_1 = 0.35 ns (47.87%), τ_2 = 9.60 ns (52.13%) for the NiTCPP MOF. Since the excited Ni-porphyrins have inherently short lifetime in pico second region[34,35], the biexponential decay of the fluorescence of NiTCPP MOF is suggesting that half of the porphyrins are Ni inserted and the rest of porphyrins are without Ni. Even in the case, the short lifetime species may be partly caused the rapid depopulation of the excited singlet state through the charge transfer. The cyclic voltammogram of the NiTCPP MOF is presented in Fig. 5S. further demonstrates the presence of well-defined anodic and cathodic peaks, signifying the reversible redox characteristics of the framework. This behavior indicates electron transfer pathways, which corroborate the PL quenching and reduced excited-state lifetime.

Photocatalytic Bacterial Inactivation

The light-assisted antibacterial performance of the NiTCPP MOF was evaluated using *S. typhimurium* as the model bacterial strain under visible-light irradiation using a 100 W Xe lamp. As illustrated in Fig. 6(a-d), the control experiments, which included bacteria alone, bacteria with NiTCPP MOF in the dark, and bacteria exposed to light without NiTCPP MOF, all resulted in significant bacterial colony growth. This suggests that neither light exposure nor the NiTCPP MOF alone had a notable bactericidal effect under the given experimental conditions. However, when the NiTCPP MOF was combined with light irradiation, bacterial colony formation was completely inhibited, indicating nearly complete inactivation. These results demonstrate that the as-synthesized NiTCPP MOF functions as an effective visible-light-responsive antibacterial photoactive material, offering great potential for photodynamic antibacterial therapy applications.

Proposed Antibacterial Photocatalytic Mechanism

Based on the experimental band structures, photophysical studies, singlet oxygen trapping assay and ORR activity, a plausible dual-pathway mechanism was proposed for the observed antibacterial activity (Fig. 7). The presence of nickel centers significantly enhances the spin-orbit coupling of porphyrin macrocycles, thus promoting the intersystem crossing from the short-lived singlet excited state to the photochemically active triplet state. Thus, the formed triplet excited state undergoes spin-allowed triplet-triplet energy transfer to the ground-state triplet oxygen, yielding singlet oxygen as the predominant reactive oxygen species (Type-II photodynamic pathway). Singlet oxygen generation was further verified by the photooxidation of anthracene-9-carboxylic acid, where the formation of the corresponding endoperoxide adduct under light irradiation (λ = 420 nm, 3.5 mW cm^{-2}) confirmed the production of $^1O_2$ (Fig. 6S). The generated singlet oxygen readily oxidizes bacterial membrane lipids, proteins, and nucleic acids, leading to bacterial cell death.

While energy transfer governs singlet oxygen evolution, the observed electronic band levels, the distinct PL quenching effect, and the reduced excited-state lifetimes of the NiTCPP MOF further support the possibility of a concurrent type-I photodynamic pathway. The photoexcited electrons accumulated in the CB (-0.7 V vs. NHE) possess sufficient reducing power to drive the single-electron reduction of dissolved oxygen to superoxide radical anion. To probe the oxygen reduction capability of the material, photocatalytic hydrogen peroxide production experiments were conducted. No detectable H_2O_2 was observed when the photocatalyst was irradiated in pure water (Fig. 7S (a, b)). In contrast, measurable hydrogen peroxide formation was obtained in an 8:2 water/methanol mixture (Fig. 8S (a, b)), where methanol acted as a sacrificial hole scavenger. These observations suggest that, even though the VB level (+ 1.3 V vs NHE) is insufficient to drive the direct oxidation of water, under the bacterial microenvironment, it provides a strong overpotential to directly oxidize the lipopolysaccharides, peptidoglycans, and surface-bound proteins of the bacterial cell envelope, whose oxidation potentials typically range between + 0.5 V and + 1.0 V vs. NHE.[36] This direct hole-mediated oxidation can initiates irreversible fragmentation of bacterial DNA.[37] Concurrently, the generated H_2O_2 readily diffuses across the lipid bilayer into the bacterial cytoplasm, generating highly destructive short-lived hydroxyl radicals (·OH) inside the cell, which causes severe lipid peroxidation, resulting in physical cell lysis.[38]

Conclusion

In summary, a NiTCPP MOF with stacked nanosheet morphology was successfully synthesized and demonstrated photocatalytic antibacterial activity against *Salmonella typhimurium.* Structural and spectroscopic analyses revealed partial in situ metalation of the porphyrin linkers by Ni, which appears to favorably influence the excited-state dynamics of the framework. Mechanistic investigations suggest that bacterial inactivation proceeds predominantly through a Type-II photodynamic pathway, in which the triplet excited state of the porphyrin sensitizer facilitates energy transfer to molecular oxygen, resulting in the generation of singlet oxygen. In parallel, the Ni-cluster nodes contribute to photoinduced charge

separation and photocatalytic oxygen reduction, supporting a secondary Type-I pathway associated with H_2O_2 generation. Furthermore, photogenerated holes in the valence band may participate in the direct oxidation of bacterial membrane components and intracellular biomolecules. The combined action of $^1O_2$, peroxide species, and hole-mediated oxidation is expected to induce oxidative stress and membrane damage, ultimately leading to bacterial inactivation. Overall, this work demonstrates that integrating porphyrinic photosensitizers with redox-active Ni-cluster nodes within a MOF architecture provides a promising strategy for coupling Type-II photodynamic processes with photocatalytic redox reactions. The findings offer valuable insights into the distinct roles of linker- and node-centered processes in reactive oxygen species generation and highlight NiTCPP MOFs as promising materials for antimicrobial application.

Declarations

Author Contribution

The manuscript was written through the contributions of all the authors. All the authors have approved the final version of the manuscript.

Acknowledgement

This work was supported by Rashtriya Uchchatar Shiksha Abhiyan (RUSA) funding (RUSA2.0/CUSAT/T1C) from the MHRD, Department of Higher Education, Government of India, the UGCBSR Start-up Grant[30-415/2018(BSR)], and the SMNRI fund from Cochin University of Science and Technology.S.N.R. thanks DST-FIST, UGC-SAP, DST-PURSE for funding support. F.K. thanks the Department of Science & Technology (DST), Government of India, for the DST-INSPIRE faculty grant (IFA19-CH320), SERB Start-up Grant (SRG/2022/002097), PURSE grant (SR/PURSE/2023/191), and ANRF PAIR Grant (ANR/PAIR/2025/000021). A.K.G. thanks the Cochin University of Science and Technology for the UJRF and USRF.The authors acknowledge STIC-CUSAT, University of Calicut, and CSIR-NIIST-Thiruvanathapuram for providing instrumentation and analytical support.

Data Availability

All data supporting the findings of this study are available within the paper and its Supplementary Information

References

1. Salam, M. A.; Al-Amin, M. Y.; Salam, M. T.; Pawar, J. S.; Akhter, N.; Rabaan, A. A.; Alqumber, M. A. A. Antimicrobial Resistance: A Growing Serious Threat for Global Public Health. *Healthcare*

(Switzerland). Multidisciplinary Digital Publishing Institute (MDPI) July 1, 2023. https://doi.org/10.3390/healthcare11131946

2. Muteeb, G.; Rehman, M. T.; Shahwan, M.; Aatif, M. Origin of Antibiotics and Antibiotic Resistance, and Their Impacts on Drug Development: A Narrative Review. *Pharmaceuticals*. Multidisciplinary Digital Publishing Institute (MDPI) November 1, 2023. https://doi.org/10.3390/ph16111615
3. Almatroudi, A. Biofilm Resilience: Molecular Mechanisms Driving Antibiotic Resistance in Clinical Contexts. *Biology*. Multidisciplinary Digital Publishing Institute (MDPI) February 1, 2025. https://doi.org/10.3390/biology14020165
4. Yaki, L. M. Bacterial Biofilms and Antimicrobial Resistance: A Global Threat. *Discover Bacteria* 2026, *3* (1). https://doi.org/10.1007/s44351-025-00035-5
5. Tanu, R.; Chaudhary, A. A.; Prakash, G.; Yasmeen, N.; Ali, M. A. M.; Raza, N.; Sharma, P. K.; Kumar, A.; Yadav, T.; Kumar, V. Exploring the Potential of Photodynamic Therapy in Overcoming Multidrug Resistance: Mechanisms, Synergies, and Clinical Advancements in Infectious Diseases. *Frontiers in Cellular and Infection Microbiology*. Frontiers Media SA 2025. https://doi.org/10.3389/fcimb.2025.1624036
6. Yan, E.; Kwek, G.; Qing, N. S.; Lingesh, S.; Xing, B. Antimicrobial Photodynamic Therapy for the Remote Eradication of Bacteria. *ChemPlusChem*. John Wiley and Sons Inc March 1, 2023. https://doi.org/10.1002/cplu.202300009
7. Ribeiro, M.; Gomes, I. B.; Saavedra, M. J.; Simões, M. Photodynamic Therapy and Combinatory Treatments for the Control of Biofilm-Associated Infections. *Letters in Applied Microbiology*. John Wiley and Sons Inc September 1, 2022, pp 548–564. https://doi.org/10.1111/lam.13762
8. Soares, J. M.; Corrêa, T. Q.; Barrera Patiño, C. P.; Gonçalves, I. S.; dos Santos, G. G.; Guimarães, G. G.; de Lima, R. V.; Lima, T. H. N.; Corrêa, B. C.; Cappellini, T. C. de S.; Silva Pereira, M. V.; Resende, A. L. F. de O.; Yakovlev, V. V.; Blanco, K. C.; Bagnato, V. S. Synergistic Paradigms in Infection Control: A Review on Photodynamic Therapy as an Adjunctive Strategy to Antibiotics. *ACS Infectious Diseases*. American Chemical Society October 10, 2025, pp 2671–2691. https://doi.org/10.1021/acsinfecdis.5c00369
9. Wang, C.; Liu, D.; Lin, W. Metal-Organic Frameworks as a Tunable Platform for Designing Functional Molecular Materials. *Journal of the American Chemical Society*. September 11, 2013, pp 13222–13234. https://doi.org/10.1021/ja308229p
10. Xue, B.; Geng, X.; Cui, H.; Chen, H.; Wu, Z.; Chen, H.; Li, H.; Zhou, Z.; Zhao, M.; Tan, C.; Li, J. Size Engineering of 2D MOF Nanosheets for Enhanced Photodynamic Antimicrobial Therapy. *Chinese Chemical Letters* 2023, *34* (9). https://doi.org/10.1016/j.cclet.2023.108140
11. Chen, M.; Zhang, J.; Qi, J.; Dong, R.; Liu, H.; Wu, D.; Shao, H.; Jiang, X. Boronic-Decorated Multivariate Photosensitive–Organic Frameworks for Combating Multi-Drug-Resistant. *ACS Nano* 2022, *16* (5), 7732–7744. https://doi.org/10.1021/acsnano.1c11613
12. Zhao, Y.; Kuang, Y.; Liu, M.; Wang, J.; Pei, R. Synthesis of Metal-Organic Framework Nanosheets with High Relaxation Rate and Singlet Oxygen Yield. *Chemistry of Materials* 2018, *30* (21), 7511–7520.

https://doi.org/10.1021/acs.chemmater.8b02467

13. Wang, J.; Zhang, X.; Liu, Y.; Wang, Z.; Wang, P.; Zheng, Z.; Cheng, H.; Dai, Y.; Huang, B. Enhanced Singlet Oxygen Production over a Photocatalytic Stable Metal Organic Framework Composed of Porphyrin and Ag. *J. Colloid Interface Sci.* 2021, *602*, 300–306. https://doi.org/10.1016/j.jcis.2021.05.087
14. Yu, W.; Zhen, W.; Zhang, Q.; Li, Y.; Luo, H.; He, J.; Liu, Y. Porphyrin-Based Metal–Organic Framework Compounds as Promising Nanomedicines in Photodynamic Therapy. *ChemMedChem*. John Wiley and Sons Ltd October 5, 2020, pp 1766–1775. https://doi.org/10.1002/cmdc.202000353
15. Wang, H.; Wu, Y.; Wang, Y.; Zou, H.; Wang, H.; Zhou, M. Vancomycin-Loaded MOF Nanoparticles for Killing Pathogenic Bacteria. *ACS Appl. Nano Mater.* 2023, *6* (11), 9874–9883. https://doi.org/10.1021/acsanm.3c01725
16. Xu, D.; Duan, Q.; Yu, H.; Dong, W. Photodynamic Therapy Based on Porphyrin-Based Metal-Organic Frameworks. *Journal of Materials Chemistry B*. Royal Society of Chemistry May 19, 2023, pp 5976–5989. https://doi.org/10.1039/d2tb02789e
17. Xu, D.; Duan, Q.; Yu, H.; Dong, W. Antibacterial Photodynamic Study on Porphyrin-Based MOF Nanoflowers under Visible Light. *ACS Appl. Bio Mater.* 2025, *8* (8), 6907–6918. https://doi.org/10.1021/acsabm.5c00652
18. Shivam, K.; Das, R.; Panda, M. K.; Mukherjee, M.; Titi, H. M.; Patra, R. Zinc–Porphyrin Terephthalate-Based Metal–Organic Framework: Structural Insights and Functional Antibacterial Properties. *ChemBioChem* 2026, *27* (8), e70286. https://doi.org/https://doi.org/10.1002/cbic.70286
19. Feng, H. X.; Zhou, Z.; Jiang, J.; Hui, Y. F.; Li, B. X.; Li, S.; Guo, H.; Tang, F. Q.; Lin, Z. J.; Yan, L. P. A Porphyrin-Based Metal–Organic Framework Nanozyme with Superior Peroxidase-like Activity for Combating Antibacterial Infections and Promoting Wound Healing. *Inorg. Chem.* 2025, *64* (7), 3541–3552. https://doi.org/10.1021/acs.inorgchem.4c05258
20. Hiremath, N.; Sanyal, P.; Jena, A. K.; Bhattacharyya, S.; Kannan, D. K.; Agarwala, P.; Upadhyaya, A. K.; Sasmal, D. K.; Sheetal, K.; Pal, S.; Lin, C.-W.; Pao, C.-W.; Negi, D. S.; K. R., R.; Korupalli, C.; Pandith, A.; Vankayala, R. Tetraniline-Engineered Nickel Molecular Frameworks for Combinatorial NIR-Triggered Photothermal and Photodynamic Cancer Therapy. *ACS Appl. Mater. Interfaces* 2026, *18* (32), 43828–43844. https://doi.org/10.1021/acsami.6c10789
21. Matsubara, C.; Kawamoto, N.; Takamura, K. *Oxo[5,10,15,20-Tetra(4-Pyridyl)Porp Hyrinatoltitanium (IV): An Ultra-High Sensitivity Spectrophotometric Reagent for Hydrogen Peroxide*; 1992; Vol. 117.
22. Kuttassery, F.; Mathew, S.; Sagawa, S.; Remello, S. N.; Thomas, A.; Yamamoto, D.; Onuki, S.; Nabetani, Y.; Tachibana, H.; Inoue, H. One Electron-Initiated Two-Electron Oxidation of Water by Aluminum Porphyrins with Earth's Most Abundant Metal. *ChemSusChem* 2017, *10* (9), 1909–1915. https://doi.org/10.1002/cssc.201700322
23. Remello, S. N.; Kuttassery, F.; Mathew, S.; Thomas, A.; Yamamoto, D.; Nabetani, Y.; Sano, K.; Tachibana, H.; Inoue, H. Two-Electron Oxidation of Water to Form Hydrogen Peroxide Catalysed by

Silicon-Porphyrins. *Sustain. Energy Fuels* 2018, *2* (9), 1966–1973. https://doi.org/10.1039/c8se00102b

24. Ishii, Y.; Nishiwaki, Y.; Al-Zubaidi, A.; Kawasaki, S. Pore Size Determination in Ordered Mesoporous Materials Using Powder X-Ray Diffraction. *Journal of Physical Chemistry C* 2013, *117* (35), 18120–18130. https://doi.org/10.1021/jp4057362
25. Ji, L.; Wang, Q.; Gong, X.; Chen, J.; Zhu, X.; Li, Z.; Hu, P. Ultrasensitive and Simple Dopamine Electrochemical Sensor Based on the Synergistic Effect of Cu-TCPP Frameworks and Graphene Nanosheets. *Molecules* 2023, *28* (6). https://doi.org/10.3390/molecules28062687
26. Zhao, M.; Wang, Y.; Ma, Q.; Huang, Y.; Zhang, X.; Ping, J.; Zhang, Z.; Lu, Q.; Yu, Y.; Xu, H.; Zhao, Y.; Zhang, H. Ultrathin 2D Metal-Organic Framework Nanosheets. *Advanced Materials* 2015, *27* (45), 7372–7378. https://doi.org/10.1002/adma.201503648
27. Herrera, F. C.; Caraballo, R. M.; Soler Illia, G. J. A. A.; Gomez, G. E.; Hamer, M. Sunlight-Driven Photocatalysis for a Set of 3D Metal-Porphyrin Frameworks Based on a Planar Tetracarboxylic Ligand and Lanthanide Ions. *ACS Omega* 2023, *8* (49), 46777–46785. https://doi.org/10.1021/acsomega.3c06153
28. Deenadayalan, M. S.; Sharma, N.; Verma, P. K.; Nagaraja, C. M. Visible-Light-Assisted Photocatalytic Reduction of Nitroaromatics by Recyclable Ni(II)-Porphyrin Metal-Organic Framework (MOF) at RT. *Inorg. Chem.* 2016, *55* (11), 5320–5327. https://doi.org/10.1021/acs.inorgchem.6b00296
29. Yang, M.; Pang, G.; Li, J.; Jiang, L.; Liang, D.; Feng, S. Fabrication of Two-Dimensional ZnO Nanostructures from Nanoparticles. *Journal of Physical Chemistry C* 2007, *111* (46), 17213–17220. https://doi.org/10.1021/jp075189g
30. Kaur, P.; Muriqi, A.; Wree, J. L.; Ghiyasi, R.; Safdar, M.; Nolan, M.; Karppinen, M.; Devi, A. Atomic/Molecular Layer Deposition of Cerium(Iii) Hybrid Thin Films Using Rigid Organic Precursors. *Dalton Transactions* 2022, *51* (14), 5603–5611. https://doi.org/10.1039/d2dt00353h
31. Guo, J.; Zhao, L.; Kong, W.; Zhu, H.; Li, W.; Liu, S.; Yu, W.; Han, X.; Wen, Z. Nanoflake Ni-MOF Anchored Octahedral Nickel-Porphyrins as a High-Performance Anode for Lithium-Ion Batteries. *Journal of Electroanalytical Chemistry* 2024, *966*. https://doi.org/10.1016/j.jelechem.2024.118397
32. Abbas, Z.; Bokhari, T. H.; Rana, Z.; Ijaz, S.; Gul, E.; Zafar, A.; Javaid, S.; Gul, M.; Maaz, K.; Karim, S.; Xiang, G.; Ahmad, M.; Nisar, A. Mesoporous Mo-Doped NiCo2O4 Nanocrystals for Enhanced Electrochemical Kinetics in High-Performance Lithium-Ion Batteries. *RSC Adv.* 2025, *15* (17), 13552–13560. https://doi.org/10.1039/d5ra00918a
33. Maeda, K.; Sekizawa, K.; Ishitani, O. A Polymeric-Semiconductor–Metal-Complex Hybrid Photocatalyst for Visible-Light CO2 Reduction. *Chem. Commun.* 2013, *49* (86), 10127–10129. https://doi.org/10.1039/C3CC45532G
34. Naumova, M. A.; Paveliuc, G.; Biednov, M.; Kubicek, K.; Kalinko, A.; Meng, J.; Liang, M.; Rahaman, A.; Abdellah, M.; Checchia, S.; Alves Lima, F.; Zalden, P.; Gawelda, W.; Bressler, C.; Geng, H.; Lin, W.; Liu, Y.; Zhao, Q.; Pan, Q.; Akter, M.; Kong, Q.; Retegan, M.; Gosztola, D. J.; Pápai, M.; Khakhulin, D.; Lawson Daku, M.; Zheng, K.; Canton, S. E. Nonadiabatic Charge Transfer within Photoexcited Nickel

Porphyrins. *Journal of Physical Chemistry Letters* 2024, *15* (13), 3627–3638. https://doi.org/10.1021/acs.jpclett.4c00375

35. Michael, C.; Fajer, J.; Shelnutt, J. A.; Holten, D. *Picosecond to Microsecond Photodynamics of a Nonplanar Nickel Porphyrin: Solvent Dielectric and Temperature Effects*; 1998.
36. Matsunaga, T.; Nakajima, T. Electrochemical Classification of Gram-Negative and Gram-Positive Bacteria. *Appl. Environ. Microbiol.* 1985, *50* (2), 238–242. https://doi.org/10.1128/aem.50.2.238-242.1985
37. Yu, Y.; Guo, S.; Lv, S.; Tian, R.; Cheng, S.; Chen, Y. Eradicating the Photogenerated Holes in a Photocatalyst-Microbe Hybrid System: A Review. *ACS Applied Materials and Interfaces*. American Chemical Society October 23, 2024, pp 56545–56554. https://doi.org/10.1021/acsami.4c12355
38. Haider, W.; Ullah, Q.; Amir, M. A.; Ahmad, N.; Farid, M.; Rahman, A.; Shezan, S. A. Heterojunction-Driven Photocatalytic Oxidation for Synergistic Pathogen and Dye Degradation in Decentralized Wastewater Systems. *Environmental Science: Water Research and Technology*. Royal Society of Chemistry June 1, 2026, pp 1693–1712. https://doi.org/10.1039/d6ew00043f

Figures

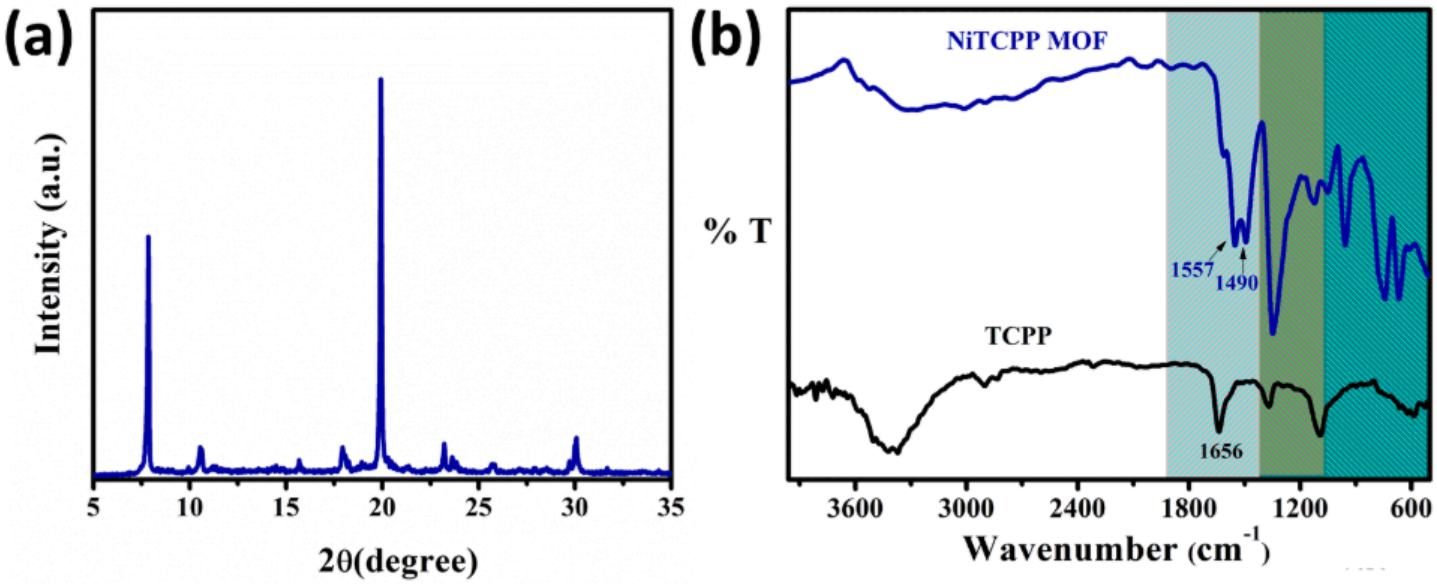


Figure 1

(a) XRD pattern and (b) FTIR spectra of NiTCPP MOF

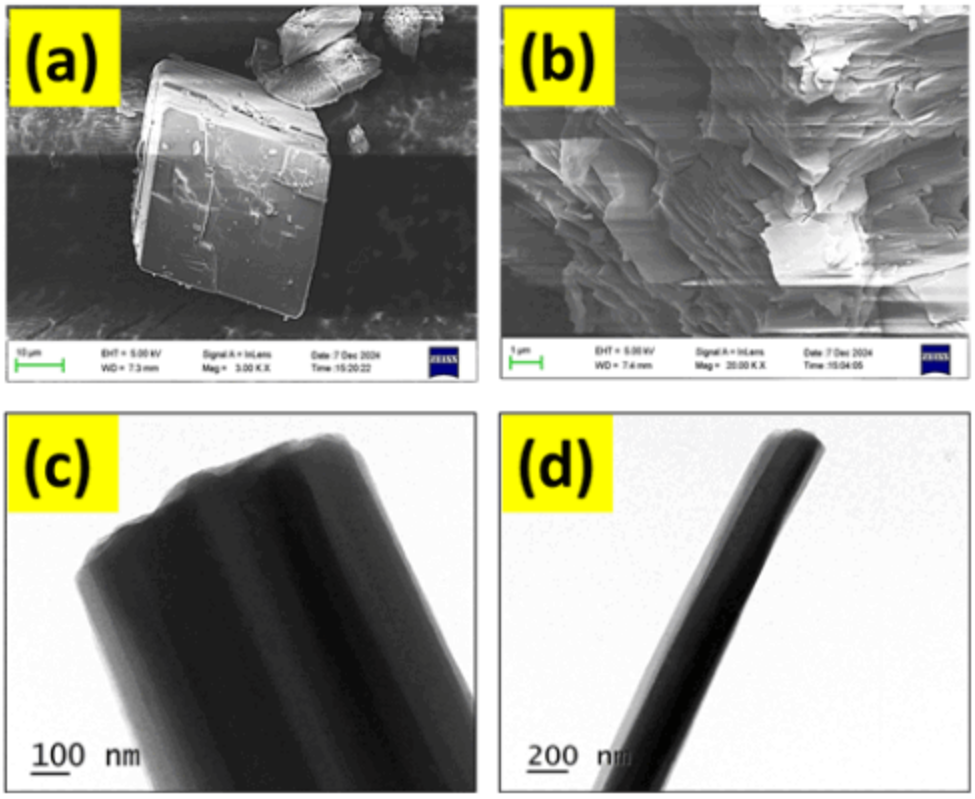


Figure 2

(a, b) FESEM images and (c, d) HR-TEM images of NiTCPP MOF

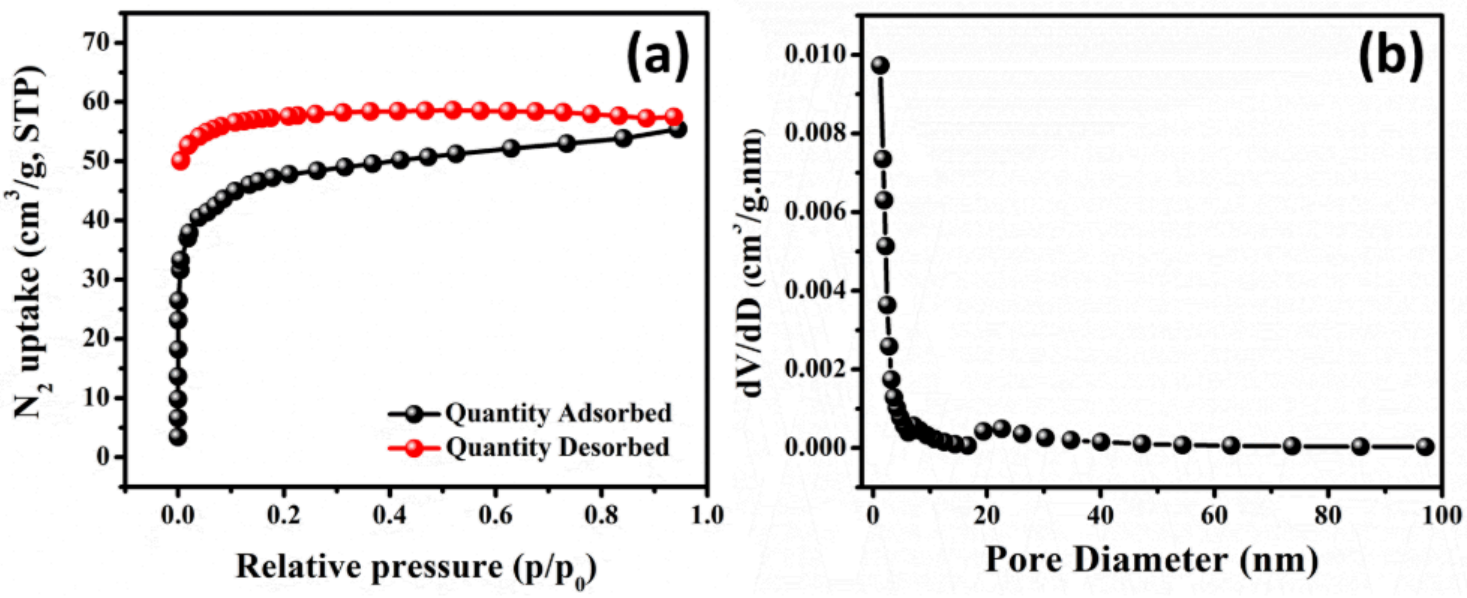


Figure 3

(a) N_2 adsorption-desorption isotherm and (b) corresponding BJH pore size distribution of NiTCPP MOF measured at 77K

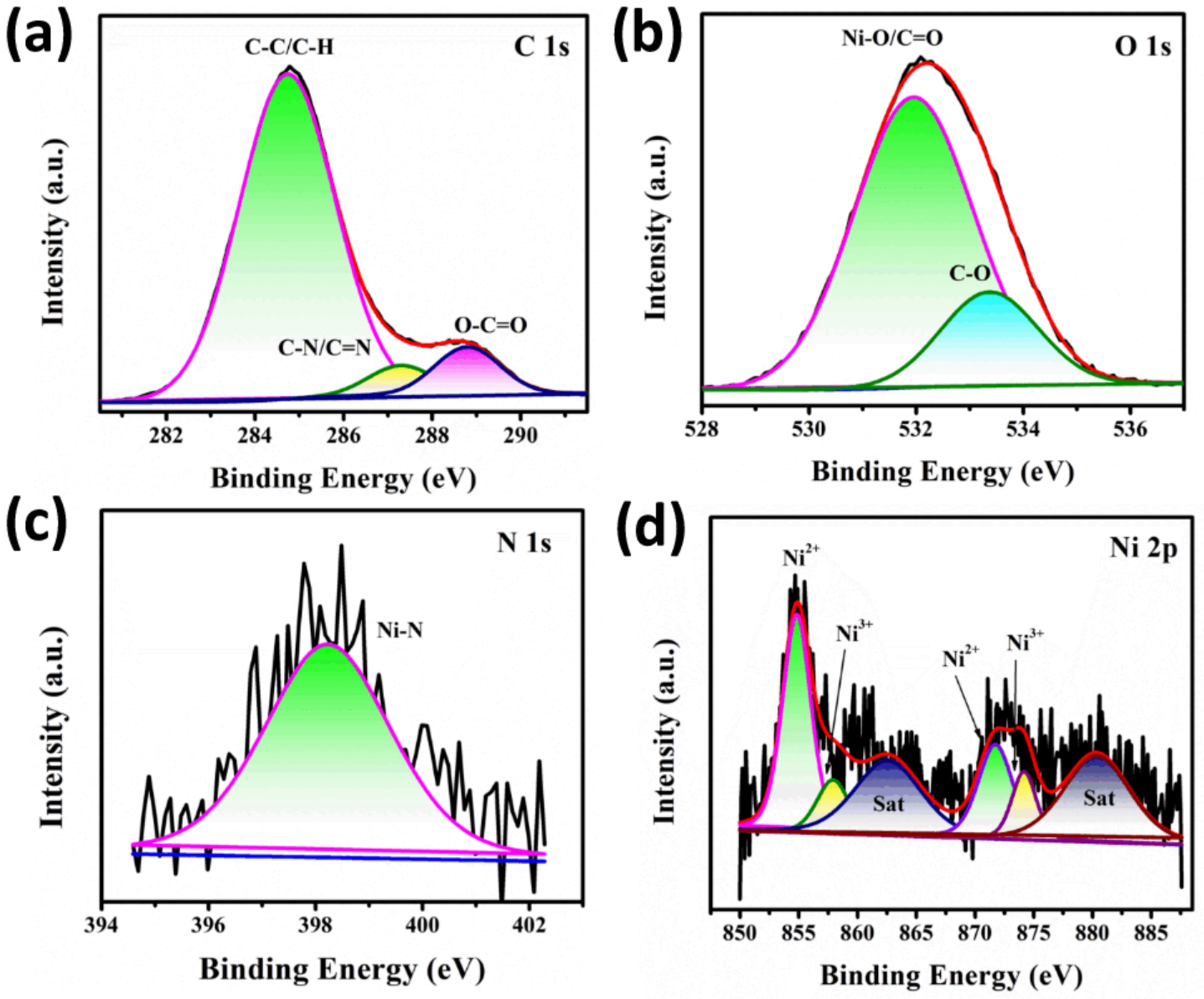


Figure 4

High-resolution XPS spectra of Ni-TCPP MOF (a) C 1s (b) O 1s (c) N 1s (d) Ni 2p

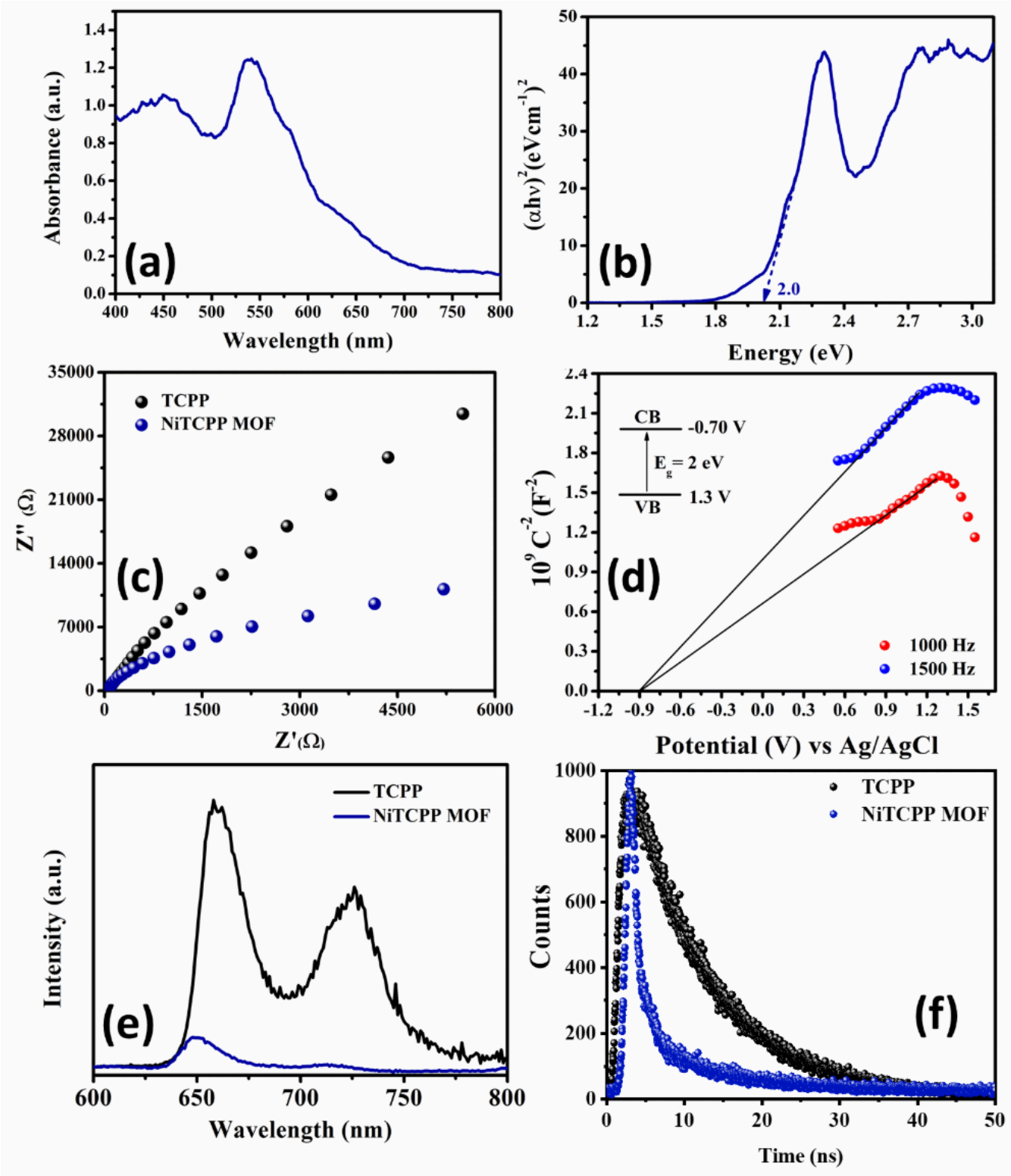
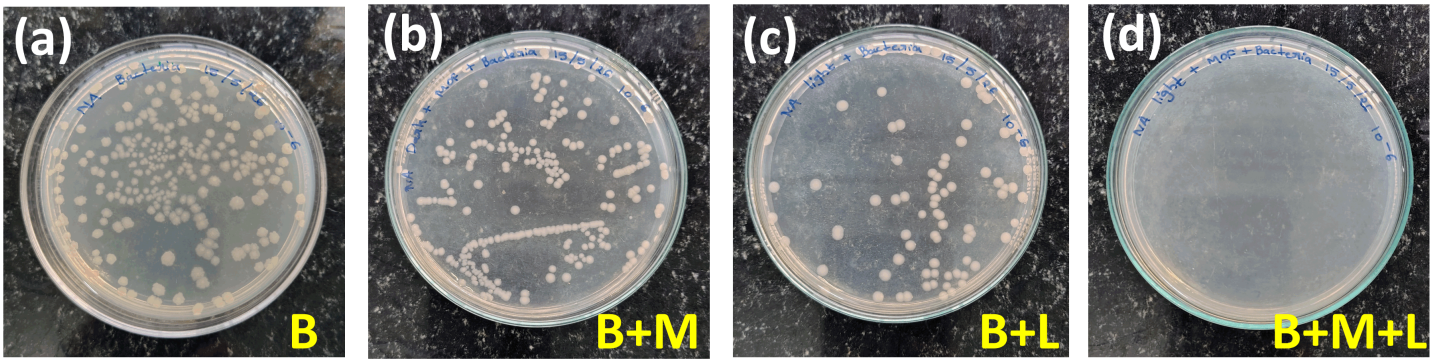


Figure 5

(a-d) UV-DRS, Tauc plot (Estimation of band gap), EIS and Mott-Schottky plot of NiTCPP MOF respectively (e) Steady-state photoluminescence spectra and (f) Time-resolved photoluminescence decay of NiTCPP MOF with excitation at 450nm



B – Bacteria only, B+M – Bacteria + MOF under dark,
B+L – Bacteria + light without MOF, B+M+L – Bacteria + MOF + light

Figure 6

*In vitro*photocatalytic antibacterial activity of NiTCPP MOF; Photographs of bacterial plates

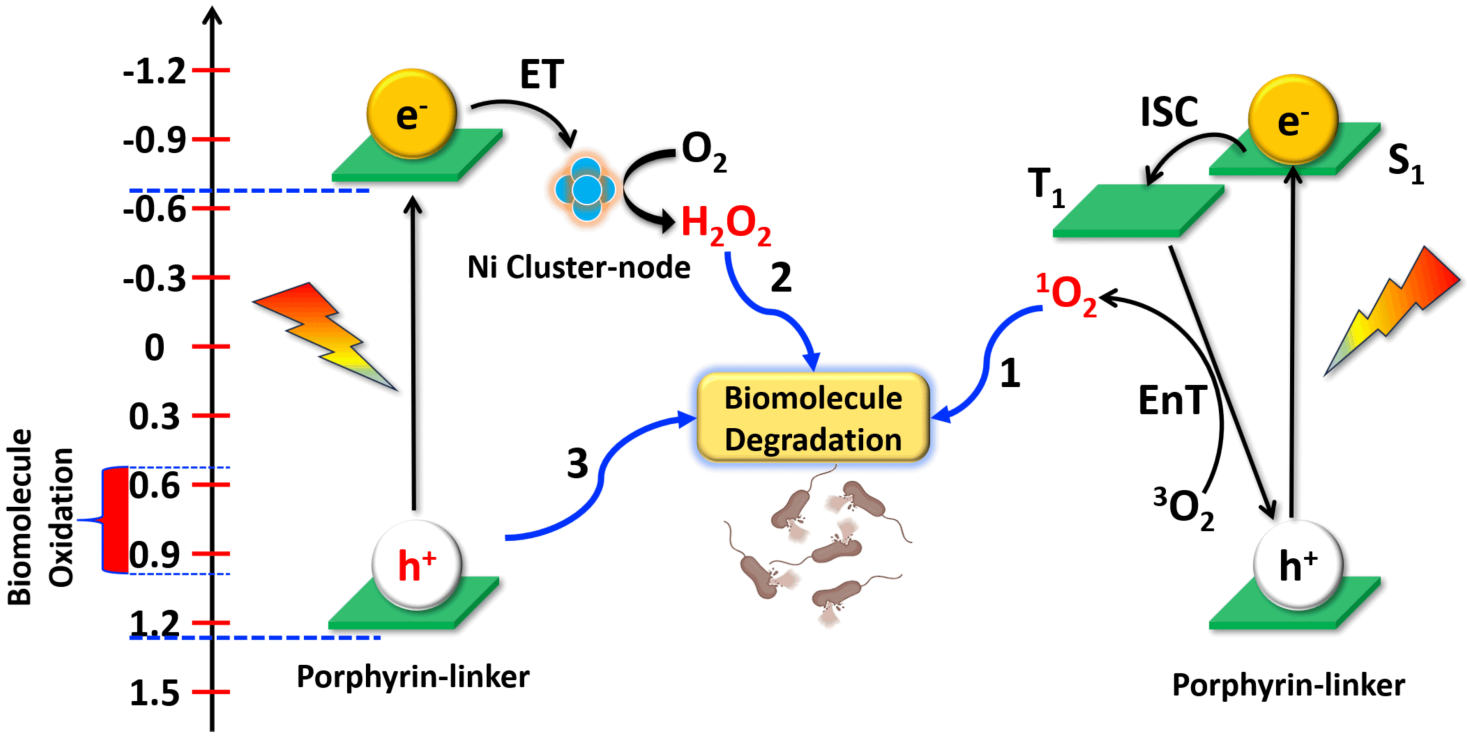


Figure 7

Proposed mechanism of photocatalytic bacterial inactivation by NiTCPP MOF, **1-** the porphyrin linkers function as light-harvesting and photosensitizing units, generating linker centered triplet excited states that produce singlet oxygen through a Type-II photodynamic pathway, **2-** photoinduced charge separation within the framework is facilitated by the Ni-cluster nodes, which promote electron transfer to dissolved oxygen and subsequent H_2O_2 formation through a Type-I pathway and **3-** photogenerated

holes residing in the VB of the NiTCPP MOF may directly oxidize bacterial membrane components and intracellular biomolecules.

Supplementary Files

This is a list of supplementary files associated with this preprint. Click to download.

- SINiMOFRCI21102026.docx
- Onlinefloatimage8.png